AIAA JOURNAL
Vol. 43, No. 7, July 2005

Strong Baroclinic Effects in a Light Jet in a Pulsed Coflow

M. Saudreau*
Institut de Mécanique des Fluides de Toulouse, 31400 Toulouse, France
J. Borée†
Ecole Nationale Supérieure de Mécanique et d'Aérothermique, 86961 Futuroscope-Chasseneuil, France
and
G. Charnay‡
Institut de Mécanique des Fluides de Toulouse, 31400 Toulouse, France

The role of strong baroclinic effects in a light jet injected into a pulsed coflow is analyzed. This case is believed to be a model situation because the induced baroclinic torque competes with the jet shear. Phase-averaged mean and turbulent properties are presented. A correct scaling is obtained from physical analysis. The striking observation is here a transition from a jet to a wake behavior during the deceleration phase. This has a dramatic influence on the evolution of the Reynolds stresses. We show that indirect effects (production terms) caused by the modification of the mean flow by the unsteady body force strongly dominate the direct coupling of the turbulence with the unsteady pressure field in this situation.

Nomenclature

A	=	butterfly valve angle, 2 deg
A_{cc}	=	acceleration number defined in Eq. (6)
B	=	butterfly valve angle, 22 deg
C	=	butterfly valve angle, 42 deg
D	=	butterfly valve angle, 62 deg
d	=	diameter, m
f	=	pulsation frequency, 75 Hz
G_{11}	=	mean pressure turbulent source term of $\overline{uu}$; see Eq. (10)
g	=	acceleration of the gravity field, 9.81 $m \cdot s^{-2}$
L	=	jet half-width, m
L_r	=	radial length scale defined by Eq. (8), m
L_z	=	longitudinal length scale defined by Eq. (8), m
P	=	pressure, Pa
P_{11}	=	turbulent production term of $\overline{uu}$; see Eq. (9)
T	=	pulsation period ($= 1/2\pi f$), s
U	=	longitudinal velocity (z direction), $m \cdot s^{-1}$
u	=	fluctuation part of U, $m \cdot s^{-1}$
u'	=	$(\overline{uu})^{1/2}$, $m \cdot s^{-1}$
$\overline{uu}$	=	longitudinal Reynolds stress, $m^2 \cdot s^{-2}$
$\overline{uv}$	=	Reynolds shear stress, $m^2 \cdot s^{-2}$
V	=	radial velocity (r direction), $m \cdot s^{-1}$
v	=	fluctuation part of V, $m \cdot s^{-1}$
W	=	azimuthal velocity (θ direction), $m \cdot s^{-1}$
w	=	fluctuation part of W, $m \cdot s^{-1}$
(z, r, θ)	=	cylindrical coordinate system
$\Delta\bar{U}$	=	velocity scale defined in Eq. (5), $m \cdot s^{-1}$
$\Delta\bar{U}'$	=	velocity scale defined in Eq. (7), $m \cdot s^{-1}$
$\Delta\bar{\rho}$	=	$\rho_\infty - \bar{\rho}$, $kg \cdot m^{-3}$
ν_t	=	turbulent diffusivity, $m^2 \cdot s^{-1}$
ρ	=	density, $kg \cdot m^{-3}$
$\overline{\rho u}$	=	longitudinal turbulent mass flux, $kg \cdot m^{-2} \cdot s^{-1}$
Σ_T	=	turbulent diffusion term; see Eq. (2)
σ_t	=	turbulent Prandtl number ($= 0.7$)
τ_a	=	pulsation timescale, s
τ_b	=	roll up of vorticity timescale, s
$\tau_j(z)$	=	mean advection timescale, s
τ_p	=	particle timescale, s

Subscripts

jet	=	jet-exit conditions
∞	=	coflowing stream

Superscripts

jet	=	jet-exit conditions
$\cdot$	=	time derivative ($\equiv \partial/\partial t$)
–	=	phase-averaged value

Received 26 April 2004; revision received 6 January 2005; accepted for publication 18 January 2005.

*Postdoctorate Student, UMR Centre National de la Recherche Scientifique/INPT-UPS 5502, Av. Camille Soula; saudreau@cerfacs.fr.

†Professor, Laboratoire d'Etudes Aérodynamiques, 1 Av. Clément Ader; jacques.boree@lea.ensma.fr.

‡Research Director, UMR Centre National de la Recherche Scientifique/INPT-UPS 5502, Av. Camille Soula.

Introduction

COMPLEX internal turbulent flows, strong density variations, high unsteadiness, and buoyancy are important aspects of the physics associated with mixture preparation in combustion chambers.[1] In such devices, accurate physical models are needed to obtain quantitative numerical predictions for variances, correlations, and therefore turbulent time- and length scales because these parameters are especially important to further compute the initiation and the development of combustion.[2] Body-force effects can be related to volumetric heat[3] or acceleration field generated by a pressure gradient along the flow[4] or other body forces. In most practical situations, flows are ducted and then subjected to imposed pressure gradient, and it is important to estimate this effect on the flow. A recent model based on vortex dynamics proposed by Sreenivasan and Prasad[5] has highlighted the role of the baroclinic torque on the mixing process of volumetric heated or accelerated jet and plume. However, they limit themselves to steady, in a time-averaged sense, spatially accelerating flows. Flows are unsteady in a lot of practical situations. The unsteadiness can arise from instabilities,[6] imposed transient phases like in pulsed jets, or from transient phases caused by the flow configuration.[7] For example, in the intake port of spark ignition engines of natural gas vehicles, the injected gaseous fuel is periodically submitted to a pulsed air flow, where acceleration can reach values of $\pm 3000g$ as a result of the opening and the closing of valves.[8]

The purpose of the present paper is to present experimental observations of strong baroclinic effects in a light jet submitted to a

pulsed coflow. A detailed analysis of the dynamical evolution of a constant density jet in the same setup was discussed in a previous paper[9] by the authors.

This case is believed to be a model situation because the induced baroclinic torque competes with the jet shear. Phase-averaged mean and turbulent properties are presented and discussed in the acceleration dominated region and during the deceleration phase.

The flow configuration and measurement techniques are described first. Experimental results are then presented and analyzed. We will particularly insist on the analysis of the transition from jet to wake flow. In this complex situation, the timescale of the perturbation is of the order of the body-force-induced timescale. Moreover, the changes in the mean flow have a dramatic effect on the turbulent field.

Description of the Flow Configuration

The experiments[10] were conducted in a square duct having a total length of 2.30 m and a cross section of 60×60 mm^2 (Fig. 1). To perform optical measurements in the upstream part of the duct, a test section was equipped with transparent sides of 128-mm length (Fig. 2). The upstream duct entrance opens out into ambient air, and the downstream duct end connects to a vacuum pump. A motorized butterfly valve is located upstream of the vacuum pump. The air channel flow is pulsed at a frequency of $f = 75$ Hz. The pulsation is tuned with the channel acoustics and corresponds with a half-wave mode. Both duct extremities are pressure nodes so that for about 30 jet diameters downstream of the duct inlet, including the test section, the coflow velocity U_∞ is quasi-uniform and varies from 5 to 30 m/s with time (Fig. 3). Resulting values of acceleration/deceleration $\dot{U}_\infty$ rise from $+400g$ to $-700g$. With a grid and a convergent-type collector placed upstream, the test section provides a flat velocity profile during the pulsation and a turbulence intensity of 1.5%. A $d_{\text{jet}} = 4$-mm-diam cylindrical tube placed in the center of the duct generates the jet. A sonic nozzle is inserted in the tube. It is located 10 cm (25 diameters) upstream of the exit of the tube in order to obtain a developed pipe flow of axial velocity equal to $U_{\text{jet}} = 60$ ms^{-1}. To fix the jet-exit velocity in the time-varying pressure field, one has to keep the volume in the tube downstream of the sonic nozzle at a minimum. In the present setup, the measured fluctuations of the jet-exit velocity are lower than 3% (Ref. 10).

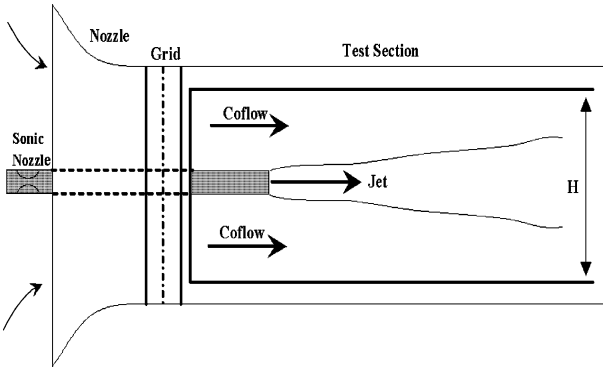

Fig. 2 Test section.

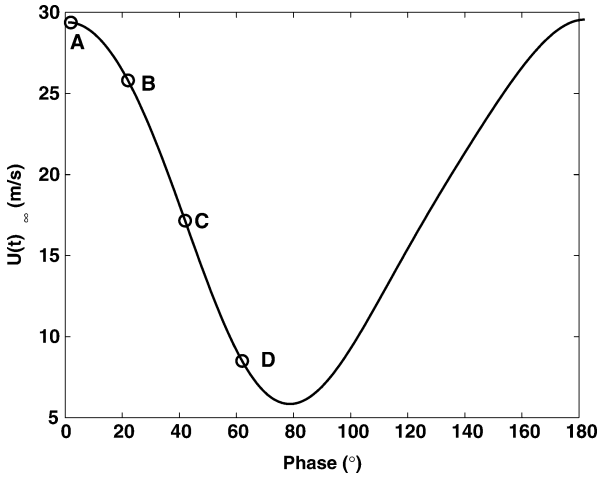

Fig. 3 Phase evolution of the coflow velocity U_∞ (A: 2 deg, B: 22 deg, C: 42 deg, and D: 62 deg).

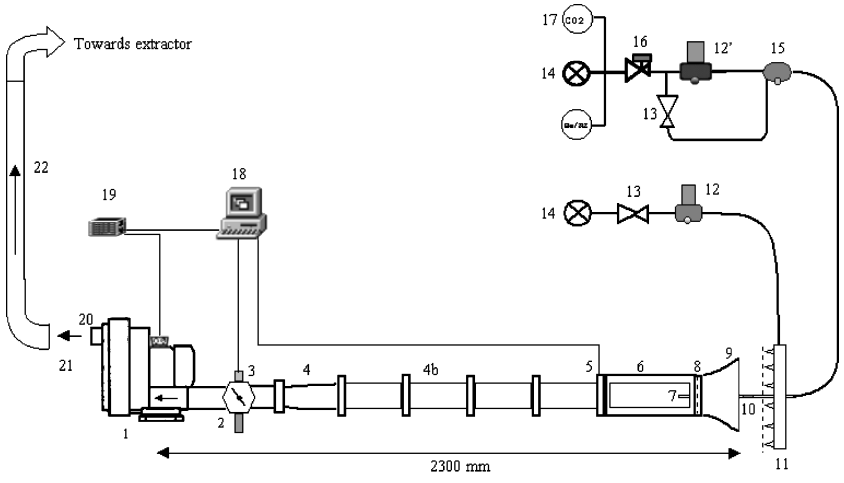

1 Vacuum pump	12 Seeding system
2 Motorized butterfly	12' Pressurised seeding system
3 Encoder	13 Flow control valve
4 Diffuser	14 Compressed air
4b Duct module	15 Pressure measurement chamber
5 Pressure sensor	16 Electropneumatic servocontrol valve
6 Test section	17 CO2 or He/N2 mixing pressurized gas
7 Coaxial jet	18 Parameters control computer
8 Turbulence generating grid	19 RFI filter equipped rotation speed switch
9 Convergent type collector	20 Exhaust
10 Sonic nozzle	21 Buffer zone
11 « spider » seeding diffusor	22 Exhaust circuit

Fig. 1 Experimental setup.

The behavior of light and homogeneous jets are compared in this paper. Density variations are obtained by considering an air channel flow and successively an air and an air–helium mixture ($\rho_{\text{mix}}/\rho_{\text{air}} = 0.55$) jet flows. The corresponding Reynolds numbers, based on outlet jet diameter, vary from 9×10^3 to 16.5×10^3, depending on the initial density. A dimensional analysis based on the initial momentum flux M_{jet} and the initial specific buoyancy flux B_{jet} permits the definition of a characteristic length scale z_b taking into account buoyancy effects.[3] In the worst situation, that is, $U_\infty = 30\ \text{m}\cdot\text{s}^{-1}$, we have $z_b/d_{\text{jet}} \approx 43$. So within the test section ($z/d_{\text{jet}} \leq 25$) the flow is momentum driven. Particular care has been taken considering experimental boundary conditions in view of numerical simulation comparison.[10]

Two-component laser Doppler velocimetry (LDV) (Dantec BSA) is used and adapted to unsteady conditions. A description of the parameters of the system is given in the Appendix. Note that a Dantec 55X12 Beam Expander is used to reduce the size of the measurement volume. The receiving optics are settled at 20 deg of off-axis angle from the incident beam to minimize the contribution of optical noise. A systematic study of the sensitivity of statistical moments and data rate to the parameters of the system was performed by Bury.[10] Two original regulated oil seeding systems were specially designed for the experiment. To limit the measurement bias[11] associated with nonhomogeneous seeding, we have achieved equal coflow and jet seeding rates. The diameter of the olive oil seed particles is of the order of 1 μm. Their time constant is thus $\tau_p = \rho_p D_p^2/18\mu \approx 3 \times 10^{-6}$ s, where ρ_p is the density of the oil particles, D_p their diameter, and μ the dynamic viscosity of air. We have checked that they are able to track accurately the turbulent flow in the present experiment. For example, downstream from 10 jet diameters and even in the most severe situation corresponding to the highest shear in the coflowing jet, one can easily estimate the ratio between this time constant and the Kolmogorov timescale. This ratio is lower than 0.2. The droplets are thus able to track all of the scales of the turbulent motion relevant for the present study. To perform ensemble averaging, an encoder is connected to the motorized butterfly valve. If we denote by an overbar $\bar{U}$ the phase average of instantaneous quantity U at a particular phase t in the period T of the pulsation, then

$$\bar{U}(\boldsymbol{x}, t) = \lim_{N \to +\infty} \frac{1}{N} \sum_{i=1}^{N} U(\boldsymbol{x}, t + iT) \tag{1}$$

The turbulence field is then deduced from the deviation between instantaneous and previous phased average fields: $u(\boldsymbol{x}, t) = U(\boldsymbol{x}, t) - \bar{U}(\boldsymbol{x}, t)$. In our case more than $N = 500$ samples per encoder degree have been used to average LDV data. Consequently, estimated statistical absolute errors for mean and rms $u' = (\overline{u^2})^{1/2}$ values are, respectively, $\Delta\bar{U} \approx 0.1.u'$, $\Delta u' \approx 0.06.u'$ with a 95% confidence level. Therefore, even in the most severe situation corresponding to the highest turbulence intensity, $\max(u'/\bar{U}) \approx 30\%$, the relative errors for mean and standard deviation values are always lower than $E_{\bar{U}} \leq 3\%$ and $E_{u'} \leq 6\%$.

Measurements of Baroclinic Effects in the Acceleration-Dominated Region

Measurements and Reynolds-averaged Navier–Stokes (RANS) computations of the dynamical response of the light and homogeneous jet during the full cycle have been performed by Bury[10] and Saudreau.[12] In a recent paper devoted to the homogeneous situation,[9] we have shown that the unsteadiness leads to a longitudinal partition of the jet: near the jet exit the flow is a quasi-steady jet flow. Jet spreading rate, axial decaying laws, and turbulent intensities are similar to the corresponding steady coflowing jet. Farther downstream the flow is unsteady. Two remarkable features were observed in the downstream unsteady region of the jet: 1) during the deceleration phase of the external stream, the flow is fully driven by the pressure gradient in the duct; 2) during the acceleration phase of the external stream, a large-scale structure similar to the structure observed in accelerated jets develops, propagates downstream, and

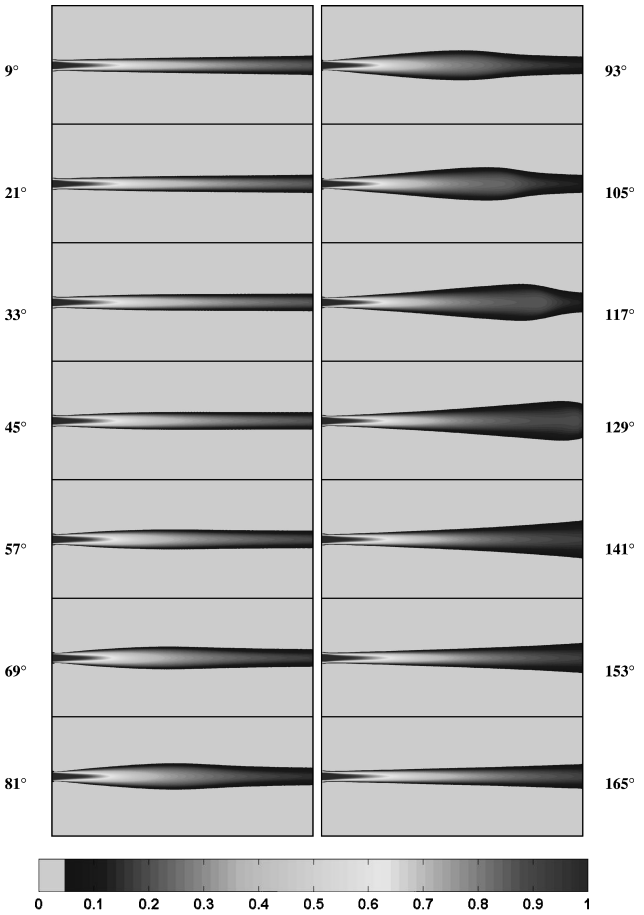

Fig. 4 Light jet evolution of the scalar field during the deceleration and the acceleration phases of the coflowing stream (RANS simulations): deceleration phase (right column) and acceleration phase (left column).

modifies considerably the spreading rate, the entrainment process, and the turbulent properties of the jet.

The goal of this paper is not to repeat the full analysis in the case of the light jet because main features are recovered[12] (Fig. 4). We will focus on the deceleration phase of the external stream. Indeed, one striking observation is that the variable density flow, driven by unsteady adverse pressure gradient, exhibits unambiguous and very strong baroclinic effects. These effects will be analyzed in the last part of the paper.

Localization of the Acceleration-Dominated Region of the Jet

The effect of gravity g can be neglected here because we deal with contrasted situations where $|\partial U_\infty/\partial t| \gg g$ and $t_p \ll t_g$; $t_p = 1/2\pi f$ is the timescale of the pulsation, and t_g is the characteristic timescale of gravity effects along the studying zone length L. We therefore face a problem of mixed convection caused by external imposed unsteadiness. The flow will be described henceforth using a cylindrical coordinate system (z, r, θ) to indicate the axial, radial, and azimuthal directions. The origin is set at the tube exit and at the center of the inner jet. The components of the instantaneous velocity field are denoted, respectively, by (U, V, W). No mean swirling motion was detected to within our measurement precision ($W \equiv 0$). The components of the instantaneous fluctuating velocity field are denoted respectively by (u, v, w). Following Eq. (1), an overbar denotes Reynolds phase averaging.

Using classical hypothesis for quasi-parallel flows, it is possible to show that, at first order, the mean momentum equation is

$$\frac{\partial \bar{U}}{\partial t} + \bar{U}\frac{\partial \bar{U}}{\partial z} + \bar{V}\frac{\partial \bar{U}}{\partial r} = \frac{1}{\bar{\rho}}\frac{\mathrm{d}\bar{P}_\infty}{\mathrm{d}z} + \frac{1}{\bar{\rho}}\Sigma_T \tag{2}$$

Σ_T includes the effects of turbulent diffusion. If Reynolds averaging is used, leading-order terms are provided by Chassaing

et al.[13] The $\mathrm{d}\bar{P}_\infty/\mathrm{d}z$ is the pressure gradient as a direct consequence of the imposed velocity variation $\bar{U}_\infty(t)$. In the external region of the uniform coflow (Fig. 2), the momentum balance reads simply $\rho_\infty(\mathrm{d}\bar{U}_\infty/\mathrm{d}t) = -\mathrm{d}\bar{P}_\infty/\mathrm{d}z$ as confinement effects can be neglected.[10] The imposed external acceleration of timescale $\tau_a = \max[\Delta U_\infty/(\partial\bar{U}_\infty/\partial t)]$, $\tau_a \approx 3$ ms here, therefore implies the presence of a longitudinal pressure gradient throughout the jet that competes with the jet internal dynamics.

The balance of mean longitudinal momentum reads

$$\frac{\partial\bar{U}}{\partial t} + \bar{U}\frac{\partial\bar{U}}{\partial z} + \bar{V}\frac{\partial\bar{U}}{\partial r} = \frac{1}{\bar{\rho}}\Sigma_T + \frac{\partial\bar{U}_\infty}{\partial t} + \frac{(\rho_\infty - \bar{\rho})}{\bar{\rho}}\frac{\partial\bar{U}_\infty}{\partial t} \quad (3)$$

With $\bar{U}_\infty(t)$, the balance of the mean excess momentum reads

$$\frac{\partial(\bar{U}-\bar{U}_\infty)}{\partial t} + \bar{U}\frac{\partial(\bar{U}-\bar{U}_\infty)}{\partial z} + \bar{V}\frac{\partial(\bar{U}-\bar{U}_\infty)}{\partial r} = \frac{1}{\bar{\rho}}\Sigma_T + \frac{(\rho_\infty - \bar{\rho})}{\bar{\rho}}\frac{\partial\bar{U}_\infty}{\partial t} \quad (4)$$

The unsteady body force appears clearly in Eqs. (3) and (4). The body-force term obviously changes sign when heavy or light jets are considered. However, this effect is not symmetrical with respect to the neutral case $\bar{\rho} = \rho_\infty$ because the same $\Delta\bar{\rho} = \rho_\infty - \bar{\rho}$ implies the same force while heavy fluids have more inertia.

In steady coflowing jets, mean advection and turbulent diffusion are in equilibrium and have therefore timescales of the same order of magnitude.[14] The convective timescale $\tau_j(z)$ can be evaluated using steady jet measurements with $\tau_j(z) = z/\bar{U}_{\mathrm{cl}}(z)$. $\bar{U}_{\mathrm{cl}}(z)$ is the mean longitudinal velocity on the jet axis at the given station z, and $\tau_j(z)$ is of the same order of magnitude as the turbulent timescale $\tau_{\mathrm{turb}} = \delta/u'$, where δ is a characteristic length scale of the jet width and u' a characteristic velocity scale of the turbulence.[15] Then, $\tau_j(z)$ increases strongly longitudinally [$\tau_j(z) \approx (z/d_{\mathrm{jet}})^2$ in a freejet]. One needs to compare the coflowing jet timescale $\tau_j(z)$ with τ_a. It seems natural to distinguish different longitudinal regions in which the response of the jet flow to the imposed unsteadiness has a different nature. In the present situation and whatever the phase, the coflowing jet develops in a quasi-steady fashion along the first diameters as $\tau_j(z) \ll \tau_a$ for $z/d_{\mathrm{jet}} < 10$. The jet timescale and the perturbation timescale are of the same order of magnitude at about $z/d_{\mathrm{jet}} \approx 15$, whereas the pulsation can dominate farther downstream.

We will concentrate on the description of the downstream region of the measurement domain during the deceleration phase. Figure 5 shows a longitudinal evolution of the different terms of Eq. (3) on the axis of an air jet—constant density case—at the phase of maximum deceleration $\{\bar{U}_\infty(t) = 17.3\ \mathrm{m\cdot s^{-1}}; [\mathrm{d}\bar{U}_\infty(t)/\mathrm{d}t] = -6600\ \mathrm{m\cdot s^{-2}}\}$. The turbulent diffusion terms are deduced as a balance. The first diameters are clearly associated with an equilibrium between advection and turbulent diffusion, whereas the competition between pressure gradient and temporal acceleration dominates the downstream region ($z/d_{\mathrm{jet}} \approx 20$). This observation validates the timescale comparisons and the longitudinal partition of the unsteady jet structure. The measurements displayed in what follows will show a clear influence of the unsteady body force in the downstream region of the light jet.

Phase Evolution of the Mean and Turbulent Velocity Field

The evolution of the radial profile of phase-averaged mean excess velocity during the deceleration is plotted in Fig. 6. The four phases A, B, C, D correspond, respectively, to butterfly valve angle degree, external velocity, and deceleration: $\{\theta, \bar{U}_\infty, [\partial\bar{U}_\infty(t)/\partial t]\}$ of 2 deg, 29.9 $\mathrm{m\cdot s^{-1}}$, $-60\ \mathrm{m\cdot s^{-2}}$; 22 deg, 26.3 $\mathrm{m\cdot s^{-1}}$, $-4500\ \mathrm{m\cdot s^{-2}}$; 42 deg, 17.3 $\mathrm{m\cdot s^{-1}}$, $-6600\ \mathrm{m\cdot s^{-2}}$; and 62 deg, 5.8 $\mathrm{m\cdot s^{-1}}$, $-1500\ \mathrm{m\cdot s^{-2}}$. The right-hand side (respectively, left-hand side) of Fig. 6 corresponds to the light jet case (respectively, air jet case).

The evolution of $\bar{U}-\bar{U}_\infty$ during the deceleration phase is very different for homogeneous and light jets. We see that the variation of $\bar{U}-\bar{U}_\infty$ is very weak in the air jet. We will show in the next part that this is an expected observation in a region of the airflow dominated by the acceleration field. On the contrary, a negative mean excess velocity is reached by the light jet at phases C and D. We also see that the relative variation of the mean excess velocity is the largest in the core of the jet where the density differences are a maximum. Equation (4) shows to us that this behavior can only be the result of the sink term caused by the body force. A physical analysis is proposed in the next part to obtain an order of magnitude of the negative mean excess velocity resulting from the adverse pressure gradient in this unsteady situation.

In Figs. 7 and 8, we compare the evolutions of the phase-averaged normal stresses for the homogeneous situation (left-hand side) and the light jet (right-hand side). The sensitivity of the turbulent field of the light jet to the deceleration is noticeable. A very strong damping of both normal stresses is observed. The picture of turbulence modification in this situation is complex. The mean pressure gradient terms [see Eq. (10) in the next section] are direct contributions. However, the modification of the mean velocity gradient implies a strong indirect effect because of the production term [see Eq. (9) in the next section]. The orders of magnitude of these contributions will be compared in the following. Figure 9 compares the evolution of the phase-averaged shear Reynolds stress in homogeneous and light jets. The right-hand side (light jet) was noisy in our experiment. It was smoothed, and Fig. 9 provides qualitative information only. The main message here is that the sign of $\overline{uv}$ changes in the light jet during the deceleration. This is again expected to have a link with the evolution of the mean lateral velocity gradient in the unsteady flow displayed in Fig. 6. From Fig. 6, an estimation of the jet half-width

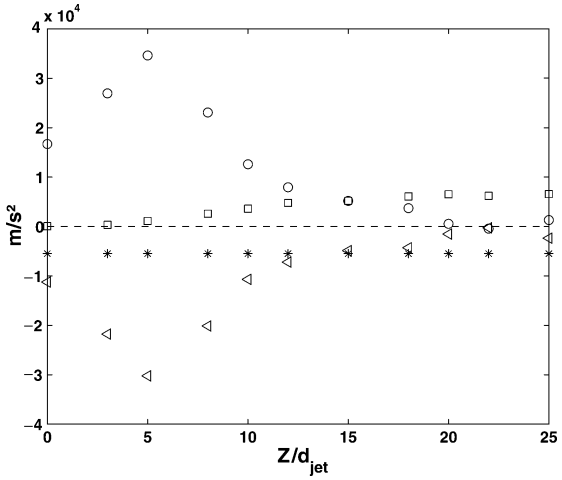

Fig. 5 Longitudinal evolution of the different terms of Eq. (3) on the axis of an air jet at the phase of maximum deceleration: □, $-\partial\bar{U}/\partial t$; ○, $-\bar{U}(\partial\bar{U}/\partial z)$; ⋆, $(\partial\bar{U}_\infty/\partial t)$; and ◁, $(1/\bar{\rho})\Sigma_T$.

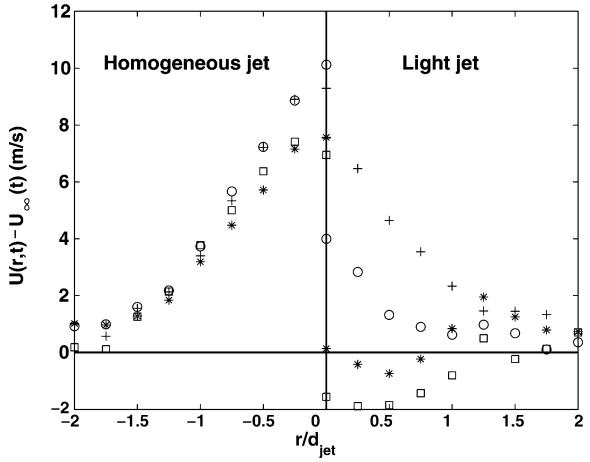

Fig. 6 Evolution of the radial profile of $[\bar{U}(r,t) - \bar{U}_\infty(t)]$ at $z/d_{\mathrm{jet}} = 20$: right-hand side, light jet and left-hand side, air jet. Phases presented: +, A; ○, B; *, C; and □, D.

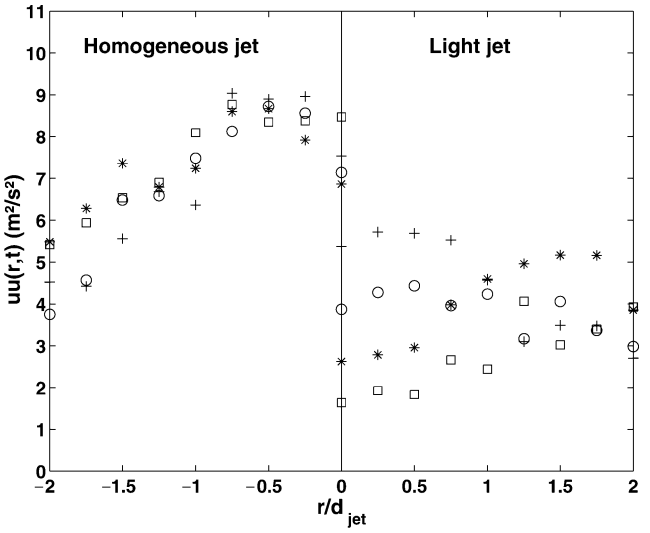

Fig. 7 Evolution of the radial profile of the longitudinal Reynolds stress $\overline{uu}(r,t)$ at $z/d_{\text{jet}} = 20$: right-hand side, light jet and left-hand side, air jet. Phases presented: +, A; ○, B; ∗, C; and □, D.

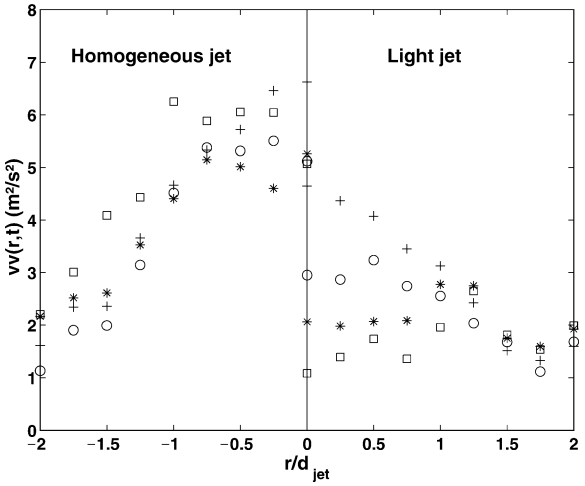

Fig. 8 Evolution of the radial profile of the radial Reynolds stress $\overline{vv}(r,t)$ at $z/d_{\text{jet}} = 20$: right-hand side, light jet and left-hand side, air jet. Phases presented: +, A; ○, B; ∗, C; and □, D.

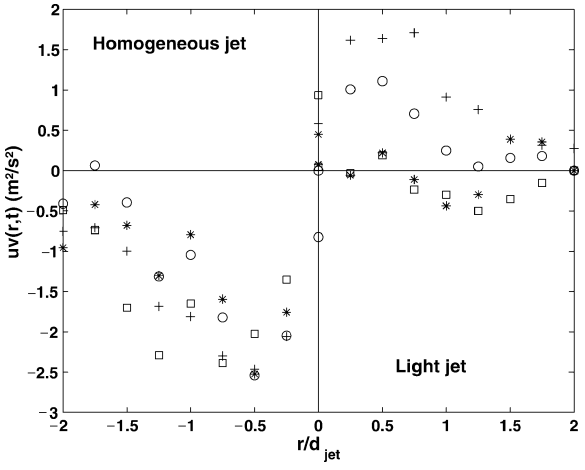

Fig. 9 Evolution of the radial profile of the Reynolds shear stress $\overline{uv}(r,t)$ at $z/d_{\text{jet}} = 20$: right-hand side, light jet and left-hand side, air jet. Phases presented: +, A; ○, B; ∗, C; and □, D.

$l(z,t)$ can be done. As usual $l(z,t)$ can be defined as the radius r, where $\bar{U}(r,z,t) - \bar{U}_\infty(t) = 0.5[\bar{U}(0,z,t) - \bar{U}_\infty(t)]$. In the homogeneous case, $l(z,t)$ is constant in time. In the light case, the jet half-width is first decreased considerably. Implications on the turbulent mixing are not straightforward because we are not in a steady situation. However, estimations can be done. In the homogeneous case, the mass of external fluid incorporated in the unsteady coflowing jet at $Z/D = 25$ is 11% lower than the amount that would be for a quasi-steady coflowing jet.[9] In the present light jet case as the jet half-width and turbulent fluctuations strongly decrease and as the mean shear is inverted, a reduction of the mixing should occur. This reduction is confirmed by RANS second-order computations and is greater than the reduction observed in the homogeneous flow.[12]

Physical Analysis and Scaling in the Acceleration-Dominated Region

It is first interesting to discuss the extreme situation in which the acceleration timescale is much smaller than the jet timescale $\tau_a \ll \tau_j(z)$. The response of a constant density flow is straightforward with $[\partial\bar{U}(r,z,t)/\partial t] = [\mathrm{d}\bar{U}_\infty(t)/\mathrm{d}t] \Rightarrow \bar{U}(r,z,t) - \bar{U}_\infty(t)$ is constant in time. This is clearly the evolution observed on the left-hand side of Fig. 6. We are therefore in a region of the flow where this hypothesis is a good approximation.

The situation is more complex in variable density flows: $\tau_a \ll \tau_j(z)$ implies a situation of "free" convection. Excess velocity scales are therefore driven by body force,[16] and the relevant parameters are timescale τ_a; body force per unit mass $\Delta\bar{\rho}/\bar{\rho}[\mathrm{d}\bar{U}_\infty(t)/\mathrm{d}t]$; and local length scale (width L) of the unsteady jet. A competition between the body force and unsteady terms in Eq. (4) results in the following velocity scale $\Delta\bar{U}$:

$$\frac{\Delta\bar{U}}{\tau_a} \approx \frac{\Delta\bar{\rho}}{\bar{\rho}}\frac{\mathrm{d}\bar{U}_\infty(t)}{\mathrm{d}t} \Rightarrow \Delta\bar{U} \approx \frac{\Delta\bar{\rho}}{\bar{\rho}}\Delta\bar{U}_\infty \tag{5}$$

This scaling is relevant only if advective terms caused by body force are not of the same order of magnitude. In a non-Galilean frame of reference moving at the velocity $\bar{U}_\infty(t)$, these terms scale with $\Delta\bar{U}^2/L$. An acceleration number A_{cc} can be defined as

$$A_{\text{cc}} = \frac{\Delta\bar{U}/\tau_a}{\Delta\bar{U}^2/L} = \frac{L}{\Delta\bar{U}\tau_a} = \frac{\bar{\rho}L[\mathrm{d}\bar{U}_\infty(t)/\mathrm{d}t]}{\Delta\bar{\rho}\Delta\bar{U}_\infty^2} \tag{6}$$

A_{cc} compares the relative distance $\Delta\bar{U}\cdot\tau_a$ covered during τ_a to the size L of the fluid parcel. If $A_{\text{cc}} \gg 1$, scaling Eq. (5) is valid because $\Delta\bar{U}\cdot\tau_a \ll L$. On the contrary, if $A_{\text{cc}} \ll 1$, a competition between the unsteady body force and advective terms results in the excess velocity scale $\Delta\bar{U}'$:

$$\frac{\Delta\overline{U'}^2}{L} \approx \frac{\Delta\bar{\rho}}{\bar{\rho}}\frac{\mathrm{d}\bar{U}_\infty(t)}{\mathrm{d}t} \Rightarrow \Delta\bar{U}' = \pm\sqrt{L\left|\frac{\Delta\bar{\rho}}{\bar{\rho}}\right|\frac{\mathrm{d}\bar{U}_\infty(t)}{\mathrm{d}t}} \tag{7}$$

Nonlinear effects[17] and roll up of the vorticity generated by the baroclinic torque indeed become dominant at the time $\tau_b = L/\Delta\bar{U}'$ (Ref. 18). Note that $A_{\text{cc}} = (\tau_b/\tau_a)^2 = (\Delta\bar{U}'/\Delta\bar{U})^2$. $A_{\text{cc}} \ll 1$ therefore implies that $\tau_b \ll \tau_a$. The dimensional analysis just presented thus enables us to distinguish two different flow regimes. In the first one, the jet flow can be considered as "frozen" at the timescale of the perturbation, and unsteady terms are dominant. In the second regime, the body force has sufficient time to induce a nonlinear behavior in the flow. This last situation is expected to have strong similarities with the development of buoyant jets in a gravitational field.[19]

Numerical simulations were performed by Saudreau[12] for this particular situation. The numerical code Melodif developed by EdF[20] was used. Favre-averaged Navier–Stokes equations were solved by using second-order modeling for the Reynolds stresses. The turbulent scalar fluxes were modeled by using a gradient hypothesis. The mean velocity and density fields are very correctly predicted by this approach. The comparison is not the goal of this

paper, but we just remark that $\Delta\bar{\rho} \approx 0.22$ is a good order of magnitude for the density differences on the jet axis at $20d_{\text{jet}}$.

If we choose the length scale L ($L \approx 5$ mm) as the global half-velocity diameter of the unsteady structure (see Fig. 6), $|\mathrm{d}\bar{U}_\infty(t)/\mathrm{d}t| \approx 6600\ \mathrm{m \cdot s^{-2}}$ and $\Delta\bar{U}_\infty = 25$ m/s, we obtain $A_{\text{cc}} = 0.23$ in the present situation. In other words, body-force effects are strong because light fluid lumps of the size L of the jet width have time to travel over the distance L and begin to distort. Using Eq. (7), an order of magnitude of the absolute value of the velocity difference is then $|\Delta\bar{U}'| \approx +2.7\ \mathrm{m \cdot s^{-1}}$. The minimum mean excess velocity measured in Fig. 5 is seen to scale with $\Delta\bar{U}'$. The estimated value is larger because the maximum value of deceleration was used in this order of magnitude analysis.

This agreement confirms the strong influence of the unsteady pressure gradient on the development of the mean flow. We observe during this deceleration a change in the sign of the mean shear rate, and the turbulence has to adapt to this change. The main features of the Reynolds-stress balance in shear flows like jets is accurately known in homogeneous[21] or inhomogeneous,[13,22] situations. In a steady air jet, the production of longitudinal normal Reynolds stress is the main positive source of turbulent kinetic energy. In this unsteady situation, production is still a major term, and the turbulent field can therefore be indirectly affected by the deceleration field via changes of the mean gradients and of production terms. On the other hand, a direct coupling of the turbulence with the unsteady mean pressure field is clear in the Reynolds-stress equations.[23] The order-of-magnitude analysis can again be used to evaluate the ratio between production P_{11} of the longitudinal Reynolds stress $\overline{\rho uu}$ and direct effect caused by the mean pressure gradient G_{11}.

We define typical radial and axial length scales associated respectively with the radial variation of the relative velocity L_r and the axial variation of the relative density field L_z. In steady situation and for a quasi-parallel flow, we have $L_r \ll L_z$ (Ref. 14). We have checked from RANS second-order computations that for our unsteady flow and in the far field of the jet this is also true:

$$L_r = \left(\frac{1}{\Delta\bar{U}'}\frac{\partial\bar{U}}{\partial r}\right)^{-1}, \qquad L_z = \left(\frac{1}{\Delta\bar{\rho}}\frac{\partial\bar{\rho}}{\partial z}\right)^{-1} \tag{8}$$

If we restrict our order-of-magnitude analysis to the main terms in the high shear region, the production term and the mean pressure gradient terms read

$$P_{11} \approx -2\overline{\rho uv}\frac{\partial\bar{U}}{\partial r} \approx -2\bar{\rho}\,\overline{uv}\frac{\Delta\bar{U}'}{L_r} \tag{9}$$

$$G_{11} = 2\frac{\overline{\rho u}}{\bar{\rho}}\frac{\partial P}{\partial z} \approx -2\overline{\rho u}\frac{\partial\bar{U}_\infty}{\partial t} \tag{10}$$

The ratio is then using Eq. (7) with $L_r \approx L$:

$$\frac{P_{11}}{G_{11}} \approx \frac{\overline{uv}}{\overline{\rho u}}\frac{\bar{\rho}\Delta\bar{U}'}{L_r(\partial\bar{U}_\infty/\partial t)} \approx \frac{\overline{uv}}{\overline{\rho u}}\frac{\Delta\bar{\rho}}{\Delta\bar{U}'} \tag{11}$$

Indeed, we have shown earlier that, in our situation, a reasonable estimate for the order of magnitude for $\Delta\bar{U}'$ is provided by Eq. (7).

Note that Reynolds averaging is used in the present order-of-magnitude estimation because this is consistent with the experimental data presented here. Mass-weighted or Favre averaging[24] is often used for the modeling procedure because the variable density closure schemes are developed as an extrapolation of constant density closure schemes.[13] The use of Favre averaging in the order-of-magnitude estimation performed here would not change the conclusion. With $U_i = \tilde{U}_i + u_i''$, where the Favre average of U_i is defined by $\bar{\rho}\tilde{U}_i = \overline{\rho U_i}$, note that the turbulent mass flux $\overline{\rho u}$ that appears in Eq. (10) is equal to $\bar{\rho}\overline{u''}$. Methods concerning the statistical averaging of variable density turbulent flows and formal relationships in second-order modeling are discussed precisely in Chassaing et al.[13] and Joly.[25]

To get an estimation of ratio (11), we use a gradient hypothesis for the turbulent momentum and mass fluxes. The use of a gradient hypothesis might be questionable in this unsteady situation. Indeed, direct contributions associated with the effect of the mean pressure gradient contribute to the turbulent shear stress and to the longitudinal turbulent mass flux themselves. An evaluation of these contributions would require an estimate of the transverse turbulent mass flux and of the variance of the density fluctuation.[13] The full problem is obviously complex with a strong coupling between all turbulent variables. We conjecture here that using the classical gradient hypothesis in the evaluation of P_{11} and G_{11} still provides relevant orders of magnitude.

One gets $\overline{uv} \approx -2\nu_t(\partial\bar{U}/\partial r)$ and $\overline{\rho u} \approx (\nu_t/\sigma_t)(\partial\bar{\rho}/\partial z)$. The ratio P_{11}/G_{11} is thus finally

$$|P_{11}/G_{11}| \approx 2\sigma_t(L_z/L_r) \gg 1 \tag{12}$$

The RANS second-order computations[12] confirm very clearly that the production terms strongly dominate the direct pressure gradient effect in this situation. The production of turbulence is noticeably damped during the transition from the jet flow to the wakelike flow. This explains the strong decrease of the normal Reynolds stresses observed in Figs. 7 and 8. Moreover, second-order computations predict a phase lag between the change of sign of the mean velocity gradient and the corresponding change of sign of the turbulent shear stress (Fig. 9). This time delay could not be accurately observed in the experiment but is expected because the turbulent field needs time to adapt to the changing situation. This time delay leads to a negative turbulent production term that cannot be taken into account by using k–ϵ modeling, for example. At the end of the deceleration phase, the mean velocity gradient is positive, and the Reynolds shear stress is negative. The production is then again positive as in steady mean wake flow.[26]

These complex behaviours illustrate the very important role of the baroclinic effects when a turbulent light jet is embedded in a strongly pulsed coflow. The baroclinic torque leads to the generation of additional mean and fluctuating vorticity within the jet. As a consequence, the mean shear rate and the production term are strongly affected during the deceleration phase. These effects have to be taken into account accurately when predicting mixing in such situations.

Conclusions

Complex internal turbulent flows, strong density variations, and high unsteadiness are key processes in the context of many industrial applications. The coflow situation corresponds to an academic situation. A longitudinal partition of the jet that separates quasi-steady regions from acceleration dominated regions is observed. For a low-density jet, we have shown that pressure gradient effects caused by acceleration imply a strong dynamical behavior in this acceleration-dominated region. In particular, a transition from a jet flow to a wake flow was observed experimentally. This implies a change of sign of the mean velocity gradients and has a dramatic effect on the turbulence field. Physical analysis has shown that the nature of this unsteady flow is different from steady plumes as the timescale of the perturbation is of the order of the body-force-induced timescale. Main contributions to the evolutions of the mean excess velocity and of the turbulent field were analyzed and deduced. Further work is presently devoted to these different aspects. In particular, the test of the performance of Reynolds-averaged Navier–Stokes (RANS) and large-eddy-simulation turbulent models in these situations is undertaken. As RANS models are concerned, the use of second-order modeling is clearly needed to have a chance to capture the main physical processes involved as the negative production term during the transient phase.

Appendix: Parameters of the LDV System

Transmitting Optics

Colors of the beams: green for U velocity/blue for V velocity.
1) Gaussian beam diameter: 1.4 mm
2) Focal length of the front lens: 310 mm
3) Beam separation: 73.7 mm
4) Diameter of the measurement volume: G: 78 μm/B: 74 μm
5) Length of the measurement volume: G: 660 μm/B: 620 μm

6) Fringe number: 36
7) Fringe spacing: G, 2.2 μm/B, 2.1 μm
8) Shift frequency: 40 MHz

Receiving Optics

1) Off-axis angle: 20 deg
2) Focal length of the front lens: 300 mm
3) Diameter of the pinhole: 100 μm
4) Magnification of the receiving optics: 3
5) Effective length of the measurement volume: 300 μm

Acknowledgments

The technical support of G. Couteau, J. J. Huc, E. Cid, S. Cazin, and C. Jarnot is gratefully acknowledged. The provision of the data by Y. Bury is also acknowledged.

References

[1]Heywood, J., *Internal Combustion Engines Fundamentals*, McGraw–Hill, New York, 1988.

[2]Fulachier, L., Borghi, R., Anselmet, F., and Paranthoen, P., "Influence of Density Variations on the Structure of Low-Speed Turbulent Flows: A Report of Euromech 237," *Journal of Fluid Mechanics*, Vol. 203, 1989, pp. 577–593.

[3]Papanicolaou, P., and List, E., "Investigations of Round Vertical Turbulent Buoyant Jets," *Journal of Fluid Mechanics*, Vol. 195, 1988, pp. 341–391.

[4]Choi, D., Gessner, F., and Oates, G., "Measurements of Confined, Coaxial Jet Mixing with Pressure Gradient," *Journal of Fluids Engineering*, Vol. 108, No. 1, 1986, pp. 39–46.

[5]Sreenivasan, K., and Prasad, A., "Vortex-Dynamics Model for Entrainment in Jets and Plumes," *Physics of Fluids*, Vol. 12, No. 8, 2000, pp. 2101–2107.

[6]Candel, S., "Combustion Instabilities Coupled by Pressure Waves and Their Active Control," *Proceedings of 24th Symposium on Combustion*, Combustion Inst., Pittsburgh, PA, 1992.

[7]Johari, H., and Paduano, R., "Dilution and Mixing in an Unsteady Jet," *Experiments in Fluids*, Vol. 23, No. 4, 1997, pp. 272–280.

[8]Raud, N., Bury, Y., Bazile, R., Borée, J., and Charnay, G., "Experimental Study of the Behavior of Confined Variable Density Jets in a Time Varying Crossflow," *Journal of Fluid Engineering*, Vol. 121, No. 1, 1999, pp. 65–73.

[9]Saudreau, M., Borée, J., Bury, Y., and G. C., "Round Turbulent Air Jet Submitted to a Pulsed Coflow," *AIAA Journal*, Vol. 42, No. 2, 2004, pp. 280–288.

[10]Bury, Y., "Structure de Jets Légers ou Lourds en Écoulement Externe Fortement Pulsé—Expérimentation Modèle du Mélange de Carburants Gazeux dans les Moteurs Alternatifs," Ph.D. Dissertation, Inst. National Polytechnique de Toulouse, No. 1703, 2000.

[11]Lehmann, B., "Laser-Doppler-Messungen in einem Turbulenten Freistrahl," DFVLR, DFVLR-Forschungsbericht, No. 86-55, Cologne, Germany, 1986.

[12]Saudreau, M., "Analysis of the Dynamics of Variable Density Turbulent Jets in a Pulsed Coflowing Stream," Ph.D. Dissertation, Inst. National Polytechnique de Toulouse, No. 1873, Toulouse, France, 2002.

[13]Chassaing, P., Harran, G., and Joly, L., "Density Fluctuation Correlations in Free Turbulent Binary Mixing," *Journal of Fluid Mechanics*, Vol. 279, 1994, pp. 239–278.

[14]Tenekees, H., and Lumley, J., *A First Course in Turbulence*, MIT Press, Cambridge, MA, 1972.

[15]Chassaing, P., *Turbulence en Mécanique des Fluides. Analyse du Phénomène dans une Perspective de Modélisation à l'Usage de l'Ingénieur*, Editions Cepadues, Toulouse, France, 2000.

[16]Tritton, D., *Physical Fluid Dynamics*, Oxford Science Publications, Oxford, 1988.

[17]Batchelor, G., Canuto, V., and Chasnov, J., "Homogeneous Buoyancy-Generated Turbulence," *Journal of Fluid Mechanics*, Vol. 235, 1992, pp. 349–378.

[18]Lundgren, T., Yao, J., and Mansour, N., "Microburst Modelling and Scaling," *Jopurnal of Fluid Machanics*, Vol. 239, 1992, pp. 461–488.

[19]Papanicolaou, P., and List, E., "Statistical and Spectral Properties of Tracer Concentration in Round Buoyant Jets," *International Journal of Heat and Mass Transfer*, Vol. 30, No. 10, 1987, pp. 2059–2071.

[20]Laurence, D., and Simonin, O., "Numerical Implementation of Second-Moment Closures and Application to Turbulent Jets," *Recent Research Advances in the Fluid Mechanics of Turbulent Jets and Plumes*, Kluwer Academic, 1994.

[21]Panchapakesan, N., and Lumley, J., "Turbulence Measurements in Axisymmetric Jet of Air and Helium. Part 1: Air Jet," *Journal of Fluid Mechanics*, Vol. 246, 1993, pp. 197–223.

[22]Panchapakesan, N., and Lumley, J., "Turbulence Measurements in Axisymmetric Jets of Air and Helium. Part 2: Helium Jet," *Journal of Fluid Mechanics*, Vol. 246, 1993, pp. 225–247.

[23]Veynante, D., and Poinsot, T., "Effects of Pressure Gradients on Turbulent Premixed Flames," *Journal of Fluid Mechanics*, Vol. 353, 1997, pp. 83–114.

[24]Favre, A., "Equations Statistiques des Fluides Turbulents Compressibles," 5^{e} Congrès Canadien de Mećanique Appliquée, New Brunswick Univ., 1975, pp. G3–G34.

[25]Joly, L., "Ecoulements Turbulents Cisaillés Libres à Masse Volumique Variable: Analyse Physique et Modélisation," Ph.D. Dissertation, Inst. National Polytechnique de Toulouse, No. 944, 1994.

[26]Uberoi, M., and Freymuth, P., "Turbulent Energy Balance and Spectra of the Axisymmetric Wake," *Physics of Fluids*, Vol. 13, No. 9, 1970, pp. 2205–2210.

A. Karagozian
Associate Editor